A TYPE-CURVE APPROACH FOR ANALYZING SHALLOW STRAIN DURING WELL TESTS

Lawrence C. Murdoch (lmurdoc@clemson.edu), Leonid N. Germanovich (leonid54@gmail.com), Soheil Roudini (sroudin@clemson.edu), Scott J. DeWolf (sdewolf@clemson,edu), Liwei Hua (lhua@clemson.edu), Robert Moak (rmoak@clemson.edu)

ABSTRACT

Strains occur at shallow depths in response to pressure changes during well tests in an underlying aquifer, and recent developments in instrumentation have made it feasible to measure essentially the full strain tensor. Simulations using poroelastic analyses indicate that shallow normal strains are approximately proportional to the logarithm of time when a well is injecting into or pumping from a uniform aquifer or reservoir. The drawdown is also a function of log time, as shown by the classic Cooper-Jacob type-curve analysis. The time when the semi-log straight line intercepts the zero-strain axis is similar to the time determined from the Cooper-Jacob pressure analysis, and it can be used to estimate hydraulic diffusivity, suggesting that horizontal strain data can be used directly to estimate aquifer properties.

This approach is applied to data measured with shallow (30 m) borehole strainmeters during an injection test at a 530-m-deep sandstone aquifer/reservoir in Oklahoma. The results show intercept times for the shallow normal strain data are essentially the same as for deep pressure data from an equivalent radial distance. The slopes of the semi-log plots of the pressure and the strain increase at the same time, suggesting that they both respond to a lateral aquifer boundary. These results confirm the type-curve approach for interpreting strain data. Significantly, though, strain was measured at shallow depths while the pressure data was measured at 530 m depth. This suggests that strain data from shallow depths could be an effective way to improve the characterization of an underlying aquifer.

INTRODUCTION

In-situ pore fluid pressures associated with fluid injection or extraction have long been measured to estimate formation properties (*Theis*, 1935; *Muskat,* 1937; *Hantush*, 1960; *Mathews and Russel*, 1967; *Earlougher*, 1977). One drawback to pressure monitoring is that the pressure signal is limited to the targeted reservoir or aquifer, so measurements require wells completed in the formation. These wells can be expensive to drill, and this limits the availability of pressure data, particularly for deep formations.

Changes in pore fluid pressure from injection or recovery deform the enveloping formation. The formation generally expands outward, away from the well, and upward, to the ground surface (*Murdoch et al.* 2020). The strain field results from changes in fluid pressure in the subsurface, so it is possible that strain data could be interpreted to obtain information similar to that estimated from analyses of pore fluid pressure. Borehole strainmeters capable of measuring small deformations are available, and new designs are under development (*Murdoch et al*. 2019). The new technology has the potential to measure strains at shallow depths that result from injection into much deeper formations. This is appealing because costs of deploying instruments in a confining unit could be significantly less than costs of drilling monitoring wells into a reservoir or aquifer.

One approach to developing a useful method of interpreting strain data is to use numerical inversion of poroelastic numerical models (*Vasco et al.* 2001; *Barbour and Wyatt*, 2014; *Murdoch et al.* 2019, 2020 and references therein), which are capable of simulating the strain field resulting from injection or extraction. Poroelastic simulations can be slow, however, and many simulations can be required for numerical inversion, so simplified interpretation methods that provide initial parameter estimates can be useful.

Transient pressure signals from hydraulic well tests have been analyzed using analytical solutions since long before computing capabilities made numerical inversion feasible. *Theis* (1935) and *Cooper and Jacob* (1946) present some of the first solutions used for well test analysis, and many others have been derived since then (*Ferris et al*. 1962; *Kruseman and deRitter*, 1970; *Streltsova*, 1988). Time series plots of dimensionless pressure are commonly referred to as "type curves" (*Ferris et al*. 1962; *Reed*, 1980; *Gringarten*, 1987). Aquifer properties (e.g., T and S), processes (e.g., leakage, delayed yield), or geometries (e.g. boundaries, reservoir shape) affect the shapes of type curves. This has led to a powerful approach where certain shapes of type curves are matched to field data to estimate aquifer properties, processes, and geometries (*Ferris et al.* 1962; *Kruseman and deRitter*, 1970; *Streltsova*, 1988). This was essential before modern computers were available for numerical inversion, but it is still important today as a way to quickly generate preliminary interpretations of well tests. Preliminary interpretations are sufficient for many applications, and they can be used as a starting point for numerical inversions.

We noticed that the strain signal measured in a confining unit during a field test, and the signal simulated using a poroelastic analysis both resembled the shape of the pressure signal in analytical solutions used for well testing. The pressure and strain both could be approximated as a function of the logarithm of time after an initial period. This is consistent with results from *Bear and Corapcioglu* (1981) who used Biot's analysis and the work of *Verruijt* (1969), to show that the radial strain at a radial distance r from a constant rate well can be approximated at late time by (from *Bear and Corapcioglu*, 1981 eq. 108)

$$\varepsilon_{rr} = \frac{QD_{\mathrm{h}}}{16\pi b} \ln\left(\frac{9D_{\mathrm{h}}t}{4r^2}\right) \tag{1}$$

where D_{h} is the hydraulic diffusivity, Q is pumping rate, and b is the aquifer thickness. Comparing (1) to the type curve analysis of *Cooper and Jacob* (1946) indicates that the radial strain and pressure in the reservoir change as the same functions of time. The solution from Bear and Corapcioglu describes deformation of the aquifer itself, but we hypothesized that radial strain in the overlying confining unit was changing at a similar time scale. It seemed feasible that this could be exploited to improve interpretation well tests by analyzing strain signals. The objective of this paper is to evaluate this hypothesis with the goal of simplifying preliminary analyses of strain data caused injection or extraction.

ANALYSES

Analytical solutions to the strains in a confining unit are currently unavailable to our knowledge, so we used numerical analysis based on poroelasticity (*Detournay and Cheng*, 1993; *Wang*, 2000) to develop baseline time series. In rectangular coordinates, conservation of momentum in a linear poroelastic medium reads (*Wang*, 2000)

$$\frac{E}{2(1+\nu)}\frac{\partial^2 u_i}{\partial x_k^2}+\frac{E}{2(1+\nu)(1-2\nu)}\frac{\partial \varepsilon_{kk}}{\partial x_i}=\alpha\frac{\partial P}{\partial x_i} \quad (2)$$

where u_i is displacement of the solid in the ith direction, E is drained Young's modulus, ν is drained Poisson's ratio, and $\varepsilon_{kk}=\partial u_k/\partial x_k$ is the volumetric strain. Hereafter, we employ the Einstein summation notation, which implies the summation over repeated tensorial indices.

Conservation of mass of the fluid at constant and uniform density leads to (*Wang*, 2000)

$$-\frac{\partial q_i}{\partial x_i}=\frac{1}{M}\frac{\partial P}{\partial t}+\alpha\frac{\partial \varepsilon_{kk}}{\partial t} \quad (3)$$

where q_i is the volumetric flux vector, P is the pore pressure change, α is the Biot-Willis coefficient, and M is the Biot modulus. Volumetric flux is given by

$$q_i=-\frac{k}{\mu}\frac{\partial}{\partial x_i}(P+\rho g x_3) \quad (4)$$

where k is the permeability, ρ is the fluid density, μ is the dynamic viscosity, g is the gravitational acceleration, and x_3 is the upward coordinate.

Geometry and boundary conditions

The geometry of the problem consists of a permeable aquifer or reservoir of thickness, b, overlain by a confining unit of thickness, d, and underlain by a confining unit of thickness, b_c (Figure 1). A well screen is assumed to fully penetrate the permeable aquifer and the volumetric flux is uniformly distributed over the well screen. The permeability of the confining layer is small and leakage out of the aquifer is set to zero. The well radius is r_w = 5 cm and lateral boundary is far from the well (R = 100 km), so there is no effect of the lateral boundary over the duration of the simulation.

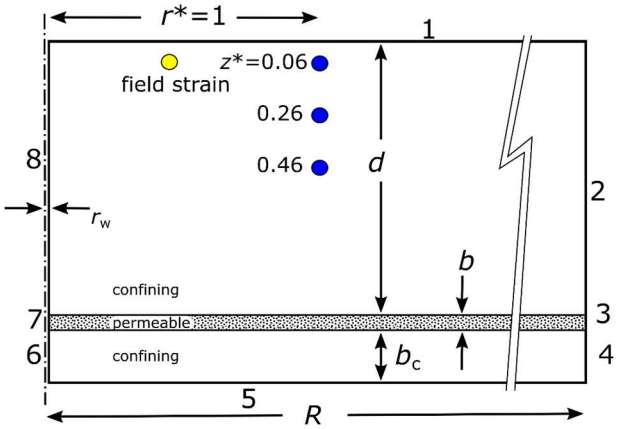

Figure 1. Cross section of model geometry assuming axial symmetry. Fluid and mechanical boundary conditions are as follows. Boundary 1: no flow and zero tractions; boundaries 2, 3, 4, 5, 6, 8: no flow and roller (zero normal displacements and zero shear tractions); boundary 7: specified flux and zero tractions. Blue dots are reference locations used in the analysis, yellow dot is the relative location of strain measurements in the field test.

The analysis is conducted using axial symmetry over domain $\{r_w < r < R, -(d+b+b_c) < z < 0\}$, which is shown in Figure 1. The boundary conditions for (2) – (4) include zero normal displacement (roller) along the bottom and outer boundary, and along the inner boundary ($r = r_w$), where it contacts the confining units. The total stress

$$\sigma_{ij} = 2G\varepsilon_{ij} + \left(K - \frac{2}{3}G\right)\varepsilon_{kk}\delta_{ij} - \alpha P\delta_{ij} \quad (5)$$

is set equal to the fluid pressure where the inner boundary contacts the reservoir (boundary 7 in Fig. 1), and the total stress is set equal to zero at the ground surface. Boundary conditions also assume zero normal pressure gradient (no flow) everywhere except where the aquifer intersects the inner boundary of the reservoir. The fluid flux is specified along the inner boundary. In (5), $K = E/[3(1 - 2\nu)]$ and $G = E/(1 + \nu)]$ are the drained bulk modulus and the shear modulus of the reservoir, respectively.

Dimensionless variables

The numerical results will be scaled using characteristic values of variables. The transformational strain (*Eshelby*, 1957) is used as the characteristic strain, and it is given by

$$\varepsilon_o = \frac{\alpha P_c}{K} \quad (6)$$

where P_c is a characteristic pressure. As the characteristic length, L_c, for a confined aquifer or reservoir, we chose the depth, d, to the top of the aquifer. The characteristic pressure during constant rate injection, Q, is

$$P_c = \frac{Q\mu}{4\pi kd} \quad (7)$$

Note that equations (6), (7) are consistent with *Bear and Corapcioglu* (1981, eq. 101).

The selected characteristic time is

$$t_c = \frac{d^2}{D_{hs}} \quad (8)$$

where the horizontal hydraulic diffusivity in the reservoir is taken as

$$D_{hs} = \frac{T}{S_s b} = \frac{k}{\mu\left(\frac{1+\upsilon}{3K(1-\upsilon)} + \frac{\varphi}{K_f}\right)} \quad (9)$$

with the uniaxial specific storage

$$S_s = \frac{1+\upsilon}{3K(1-\upsilon)} + \frac{\varphi}{K_f} \quad (10)$$

and transmissivity

$$T = \frac{kb\gamma}{\mu} \quad (11)$$

The first term in (10) is the inverse of the uniaxial bulk modulus (Wang, 2000), which assumes incompressible grains.

The dimensionless time, pressure change, and strains follow respectively as

$$t^* = \frac{t}{t_c}, \quad P^* = \frac{P}{P_c}, \quad \varepsilon_{ij}^* = \frac{\varepsilon_{ij}}{\varepsilon_o} \tag{12}$$

and dimensionless coordinates are given by

$$r^* = \frac{r}{d}, \; z^* = \frac{z}{d} \tag{13}$$

In the following, all other parameters of the length dimension will also be normalized by *d* and marked by the asterisk. For example, the dimensionless reservoir thickness

$$b^* = \frac{b}{d} \tag{14}$$

Porous Medium Analysis

The poroelastic analysis was compared to the numerical solution where storage change is assumed to be proportional to pressure change, which is the typical assumption for the analysis of hydraulic well tests. This approximation is called the *porous medium analysis*, when the storage term, $\partial\varepsilon_{kk}/\partial t$ in (3) is ignored and the uniaxial specific storage (10) is employed as the inverse Biot modulus, $1/M$. The porous medium analysis was conducted using the same geometry and boundary conditions as the poroelastic analysis. In both cases, $r_w^* = 2x10^{-4}$, $R^* = 200$, $b^* = 0.06$, $b_c^* = 0.2$.

The analyses were compared to the late-time drawdown in a confined reservoir, which is given by (*Jacob*, 1946; *Verruijt*, 1969)

$$P = \frac{Q\mu}{4\pi kb}\ln\left(\frac{9D_{hs}t}{4r^2}\right) = \frac{P_c}{b^*}\ln\left(\frac{9}{4}t_p^*\right) \quad (t_p^* \gg 1) \tag{15}$$

where

$$t_p^* = \frac{t^*}{r^{*2}} \tag{16}$$

is the dimensionless timescale of pressure diffusion over distance *r**. Taking the product of time and the derivative of (15) with respect to time

$$t\frac{\partial P}{\partial t}\frac{1}{P_c} = t^*\frac{\partial P^*}{\partial t^*} = \frac{1}{b^*} \tag{17}$$

Therefore,

$$b^* t\frac{\partial P}{\partial t}\frac{1}{P_c} = b^*\frac{\partial P^*}{\partial \ln t^*} = 1 \quad (t_p^* \gg 1) \tag{18}$$

In the spirit of the type-curve approach (*Ferris et al.* 1962; *Reed*, 1980), a time dependence of function f will be analyzed below using a semi-log plot, which is equivalent to the parametric representation of f as $f(u)$, where $u = \log_{10} t$. The slope of function f at time t (*Bourdet et al*., 1989) in the (u, f) coordinates (i.e., in the semi-log plot) is given by

$$\frac{df}{du} = \frac{df}{d\,\mathrm{lo}_{10}\,t} = t\frac{df}{dt}\ln 10 = \frac{df}{d\ln}\ln 10 \tag{19}$$

and will be called a semi-log slope of function f at time t. Hence, equation (18) states that the semi-log slope of the reservoir pressure, scaled by $(\ln 10)P_c/b^*$, approaches unity at late-time drawdown/injection pumping stages.

PRESSURE TRANSIENTS

The results indicate that the pressure predicted using the poroelastic analysis is within a few percent of the pressure predicted by the porous medium analysis (Figure 2) when the uniaxial specific storage coefficient is used in the porous medium analysis.

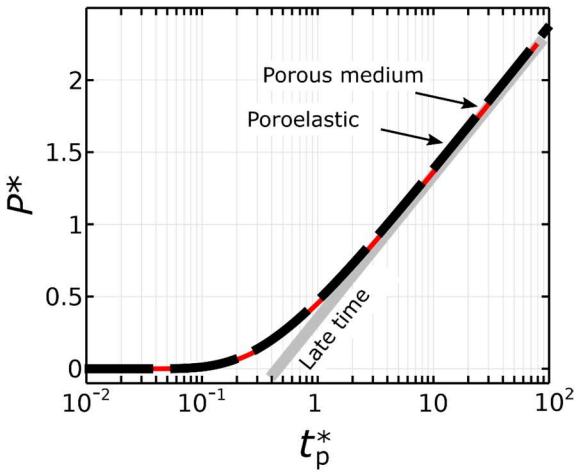

Figure 2. Dimensionless pressure as a function of dimensionless time at $r^* = 1$. Red line is porous medium analysis using the uniaxial specific storage (10), dashed line is poroelastic analysis, grey line is based on the late-time drawdown approximation (15).

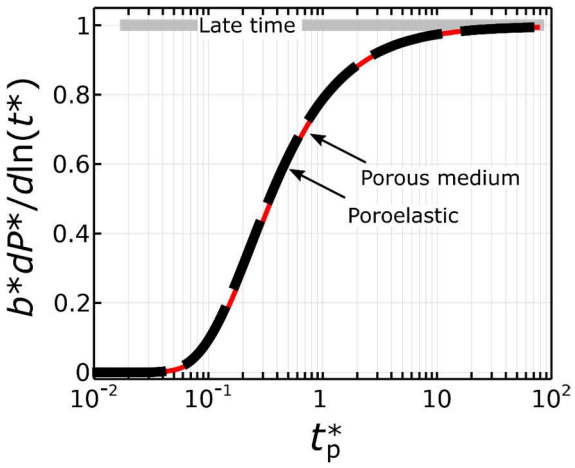

Figure 3. Scaled semi-log slope, $b^*dP^*/d(\ln t^*)$, of reservoir pressure at r^*=1 for analysis assuming porous medium with uniaxial specific storage (red) and poroelastic analysis (black dashed).

The scaled, semi-log derivative of both solutions increases and approaches unity (Figure 3), which is consistent with equation (18). At r^*=1, the approach to unity occurs over roughly an order of magnitude in time, between approximately $\mathbf{1 < t_p^* < 10}$.

STRAIN TRANSIENTS

At shallow depths, the horizontal strains increase (becomes more tensile) and become an approximate linear function of the logarithm of time, similar to the pressure in the reservoir (eq. (15) and Figure 4). At radial distances approximately greater than the depth (r^*>1), the radial strain decreases initially as the formation is initially compressed, but then the sign reverses and it becomes tensile with increasing time. The vertical strain is compressive and it also increases as a log function of time at t^*>1 (Figure 4).

The analyses were conducted using three different depths ranging from a few percent to roughly $d/2$ (Figure 4). The plots showing a normal strain component from different depths are difficult to distinguish from each other (Figure 4 and 5), which indicates that the normal strains are only slightly sensitive to depth within zone that was evaluated {$0.05 < r^* < 2.5$; $-0.06 < z^* < -0.46$} (Figs. 4 and 5). The borehole tilt, $\omega_{rz} = \partial\varepsilon_{rr}/\partial z$, is highly sensitive to depth, however. Tilt changes sign over this depth range, with tilts occurring away from the well at z^*=0.06 and toward the well at z^*=0.46, and tilts are negligible at the middle depth of z^*=0.26 (blue lines in Figure 4).

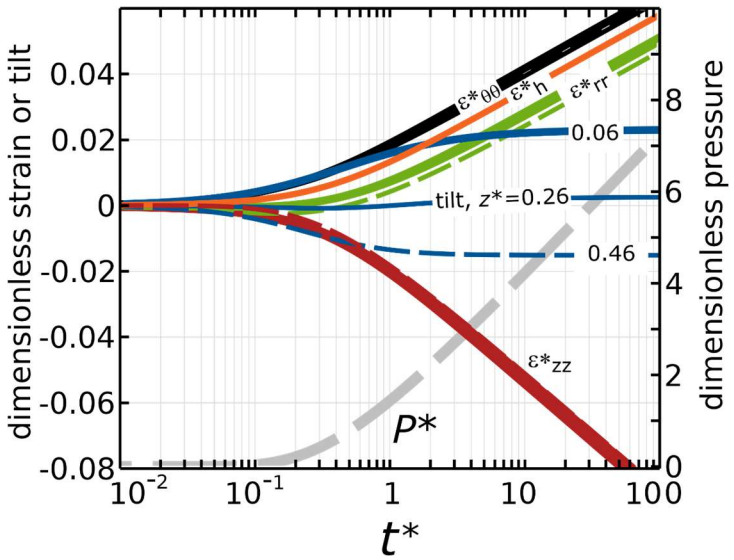

Figure 4. Dimensionless strain, tilt and pressure as functions of time at different depths at r^*=1. Heavy line is at z^*=0.06, thin solid line is z^*=0.26, dashed line is at z^*=0.46. Grey dashed line is pressure, P^*. Red lines are vertical strain, ε^*_{zz}, green is radial strain, ε^*_{rr}, black is circumferential strain, $\varepsilon^*_{\theta\theta}$, blue is tilt, $\omega^*_{rz} = \omega_{rz}/\varepsilon_0$, orange line is average horizontal strain, ε^*_h.

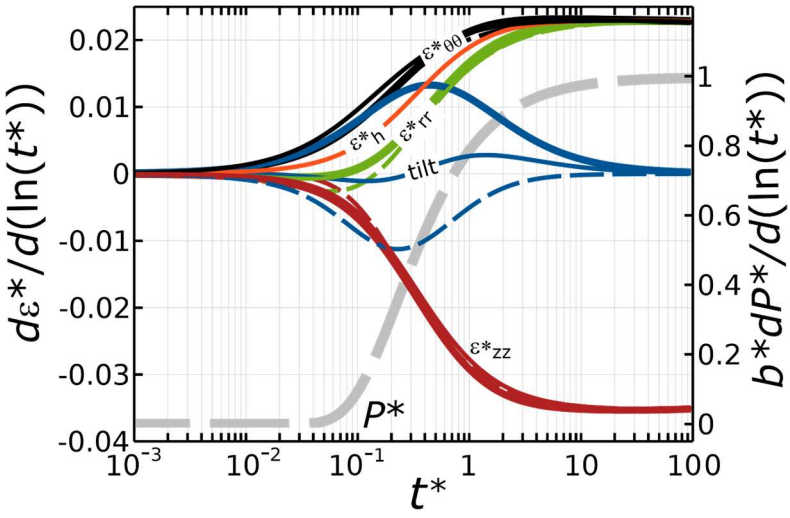

Figure 5. Scaled semi-log slopes of strains, tilt and pressure as functions of time at different depths at r^* = 1, based on the data used for plots in Figure 4. Heavy line is at z^*=0.06, thin solid

line is z^*=0.26, dashed line is at z^*=0.46. Grey dashed line is pressure, P^*. Red line is vertical strain, ε^*_{zz}, green is radial strain, ε^*_{rr}, black is circumferential strain, $\varepsilon^*_{\theta\theta}$, blue is tilt, $\partial\varepsilon_{rr}/\partial z$, orange line is average horizontal strain, ε^*_h.

190

191 **Semi-log slope**

192 The semi-log slope of the scaled horizontal strain increases and becomes constant over
193 the range of $1 < t^* < 10$ for $r^* < 2$ (Figure 5). Interestingly, the radial and the circumferential
194 strain follow the same semi-log slope (slope = 0.023). The semi-log slope of the average
195 horizontal strain, $\varepsilon_h = (\varepsilon_{rr} + \varepsilon_{\theta\theta})/2$, is the same as the radial and circumferential strains. The
196 semi-log slope of the vertical strain is steeper (0.035), but it also appears (Figure 5) to be
197 essentially independent of location within the evaluated zone. The results from Figure 5 indicate
198 that

199
$$\frac{1}{\varepsilon_o}\frac{d\varepsilon_{ij}}{d\log_{10} t} = t\frac{\ln 10}{\varepsilon_o}\frac{d\varepsilon_{ij}}{dt} = \begin{cases} 0.023 & (ij = rr) \\ 0.023 & (ij = \theta\theta) \\ 0.035 & (ij = zz) \end{cases} \quad (20)$$

200 It follows that the transformation strain can be estimated from the semi-log slope of the strain
201 data for $t^* > 1$ and $r^* < 2$ as

202
$$\varepsilon_o = \frac{1}{0.023}\frac{d\varepsilon_{rr}}{d\log_{10} t} = \frac{1}{0.023}\frac{d\varepsilon_{\theta\theta}}{d\log_{10} t} = \frac{1}{0.035}\frac{d\varepsilon_{zz}}{d\log_{10} t} \quad (21)$$

203

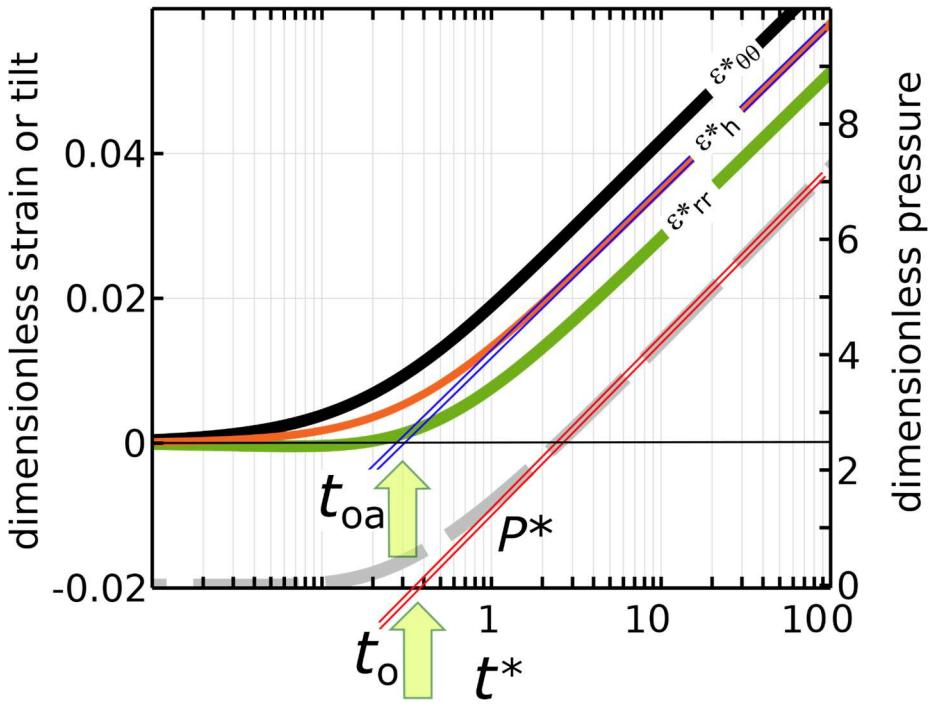

Figure 6. Dimensionless strains, ε_{ij}^*, and pressure, P^*, as functions of dimensionless time, t^*. Green line: ε_{rr}^*, black: $\varepsilon_{\theta\theta}^*$, orange: ε_h^*, grey dashed line: P^*. Arrows point to t_o and t_{oa}.

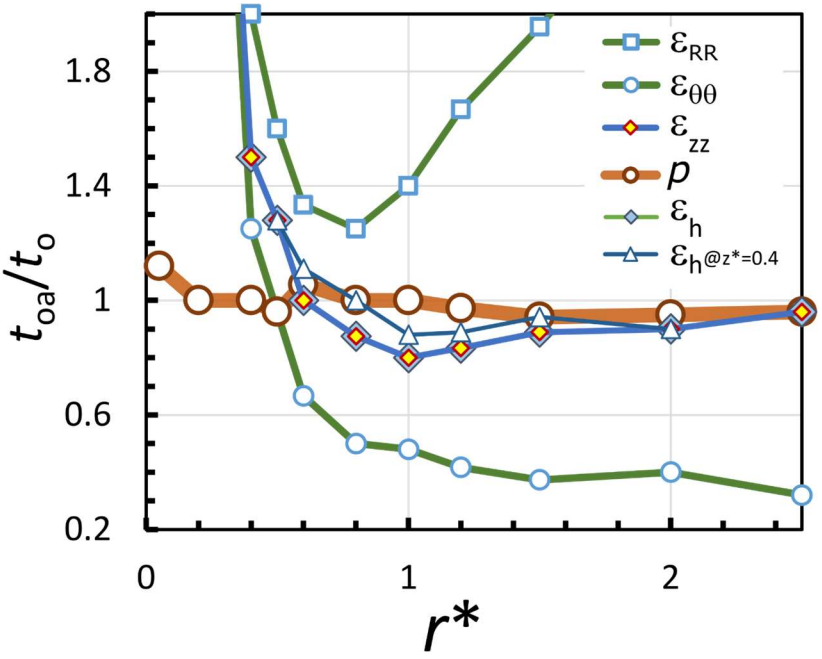

Figure 7. Ratio of the intercept time, t_{oa}, determined using strain data and t_o determined from pressure data as a function of r^*. All strain data were computed at $z^* = 0.06$, and ε_h was also computed at $z^* = 0.46$ (as noted).

204

205 **First semi-log intercept**

206 The portion of the pressure and strain data that follows a semi-log straight line can be
207 extrapolated backward in time to intersect the abscissa. When this is done with the pressure
208 signal described by (15), the intersection occurs at

209 $$t_o = \frac{4S_s b r^2}{9T} = \frac{4r^2}{9D_{hs}} \tag{22}$$

210 and it follows that the hydraulic diffusivity can be estimated as

211 $$D_{hs} = \frac{4r^2}{9t_o} \tag{23}$$

212 The normal strain data were extrapolated to the time when zero strain occurs, t_{oa}, and this time
213 was compared to t_o determined from the pressure analysis at different radial distances. The strain
214 was measured at shallow depth, z^*=0.06, whereas the pressure was measured in the underlying
215 aquifer at the same radial distance. Both times were determined by manually fitting a line to
216 pressure or strain data determined using the numerical analysis (Figure 6).

The results (Figure 7) indicate that t_{oa} determined from the strain data is similar to t_o from the pressure data in some cases. In particular, t_{oa} determined from the vertical strain and from the average horizontal strain is within $0.8t_o < t_{oa} < t_o$ for measurement locations greater than approximately $r^*>0.5$. The semi-log straight lines for the vertical strain and the average horizontal strain intersect at zero strain, and so they give the same value of t_{oa} for all the cases that were evaluated. Time t_{oa} from radial strain is greater than t_o, whereas t_{oa} from the circumferential strain is less than t_o for $r^*>0.5$. Values of t_{oa} are greater than t_o for normal strains in the vicinity of the well ($r^*<0.5$) (Figure 7).

Composite aquifer

The analysis was revised by modifying the reservoir to include an outer zone at a uniform radial distance with properties that contrast from the inner zone near the well. This is a simple case of a heterogeneous, composite reservoir with a well at the center (*Olarewaju and Lee*, 1987), so it was analyzed using the axially symmetric model outlined above. An example case was evaluated where the zone boundary is at $R = 10$ km and the permeability of the outer zone is 1/3 of permeability of the zone near the well. The results show that the pressure follows a straight line for $t^*<10^2$, and then it steepens and straightens to constant slope for $t^*>10^3$ (Figure 8a). This behavior of the pressure is well known (*Streltsova*, 1988) and can be interpreted to estimate the mobility ratio

$$M = \frac{k_1\mu_2}{k_2\mu_1} = \left(\frac{s_2}{s_1}\right)_{\mathrm{p}} \tag{24}$$

where the subscript indicates the inner (subscript 1) and the outer (subscript 2) zones, and $(s_2/s_1)_{\mathrm{p}}$ is the ratio of the slope of the second semi-log straight segment, s_2, to the semi-log slope of the first segment, s_1, in the pressure signal (Figure 8a). The ratio $(s_2/s_1)_{\mathrm{p}} = 3.00$ for Figure 8a and the mobility ratio used in the simulation is 3.00, which confirms this interpretation.

The semi-log slope of the strain signal also increases over the interval $10^2 < t^* < 10^3$ (Figure 8). The ratio $(s_2/s_1)_{\varepsilon} = 2.97$ for the strain signal in Figure 8b, which is similar to $(s_2/s_1)_{\mathrm{p}}$. A suite of analyses was conducted with mobility ratios over the range $0.5 < M < 12$, and the results indicate that $(s_2/s_1)_{\varepsilon} = (s_2/s_1)_{\mathrm{p}}$ with a correlation of 0.991.

The similarity between the strain and pressure signals was further evaluated by simulating a suite of scenarios with contrasts in Young's modulus between the inner and outer zones. The results indicate that contrasts in E affect the transition period, but the equilibrated slope is unaffected. Specifically, $s_{2\varepsilon} = 0.068$ for all values of E (Figure 8). This result is consistent with the pressure response in composite aquifers (*Olarewaju and Lee*, 1987), where the equilibrium slope $s_{2\mathrm{p}} = 3$ is independent of the specific storage. This indicates that the mobility ratio determined from normal strains $(s_2/s_1)_{\varepsilon}$ will be essentially the same as that determined by analyzing the pressures $(s_2/s_1)_{\mathrm{p}}$.

The distance to the boundary between the inner and outer zones of a composite reservoir can be estimated using (*Streltsova*, 1988; eq. 5.66)

$$L_b = 1.5\sqrt{D_{\mathrm{h1}}t_b}\; D_{\mathrm{hR}}{}^{-a/2} \tag{25}$$

where t_{b} is the time when the semi-log straight lines intersect, and D_{h} is hydraulic diffusivity and

256 $$a = \frac{T_R}{T_{R-1}} \quad (26)$$

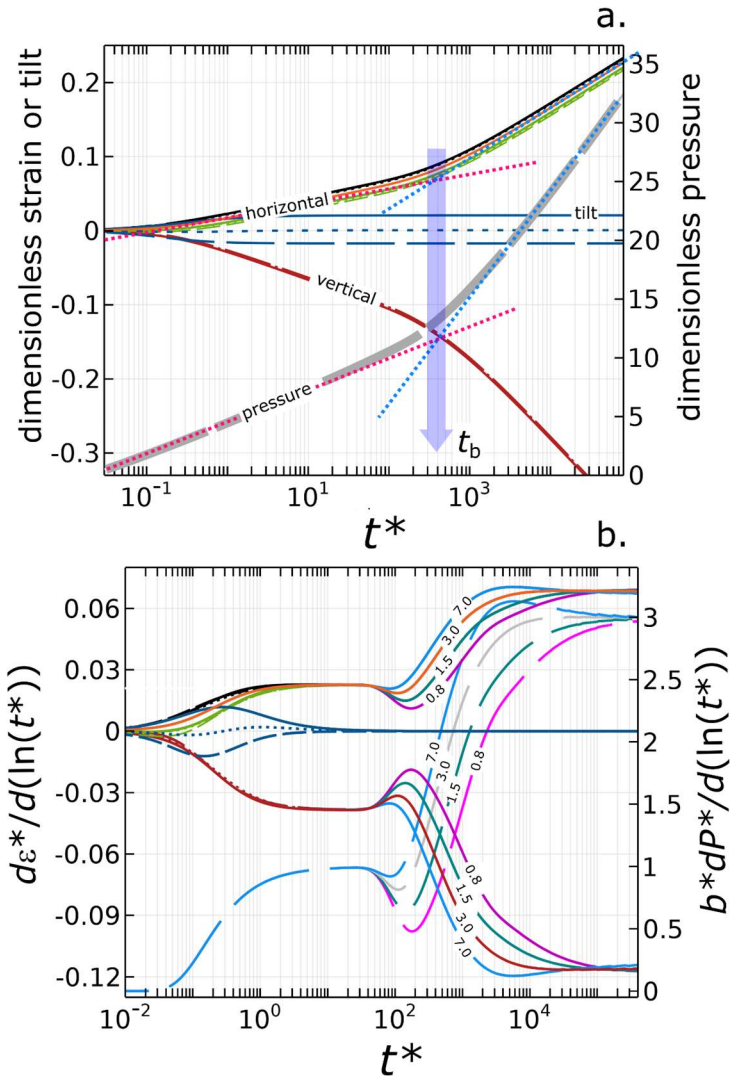

Figure 8. a.) Dimensionless pressure, P^* (grey dash), strains, ε_{ij}^*, and borehole tilt, $\omega_{rz}^* = \omega_{rz}/\varepsilon_0$, (blue) computed at $r^* = 1$ in a composite radial reservoir where the permeability decreases by a factor of 3 at $r = 10$ km. Radial, ε_{rr}^* (black), and circumferential, $\varepsilon_{\theta\theta}^*$ (green), strains are similar to the average horizontal strain, ε_h^* (orange). Results from different depths (heavy solid line is at z*=0.06, dotted line is at z*=0.26, dashed line is at z^*=0.46) are nearly indistinguishable. Purple arrow points to t_b in equation (25). b.) Semi-log slope of strains (solid), tilt (solid), and pressure (dashed), where Young's modulus of the inner region is $E = 3$ GPa and Young's modulus of outer zone is E =0.8, 1.5, 3, and 7 GPa (labeled).

257

258 where $T_R = T_1/T_2$, $D_{hR} = D_{h1}/D_{h2}$, and the subscripts 1 and 2 indicate the inner and outer regions,
259 respectively. The value of t_b in Figure 8 is identified by the intersections of red lines fit to the
260 first semi-log period and blue lines fit to the second semi-log straight period. Time t_b determined

from the pressure data is essentially the same as t_d from the strain data. This finding was confirmed using a suite of analyses with different mobility ratios, which are not shown here.

FIELD EXAMPLE

The analysis outlined above was applied to an injection test conducted at well 9A in the North Avant Field, Osage County, Oklahoma (*Murdoch et al*., 2019, 2020). Well 9A intersects the Bartlesville sandstone at a depth of 530 m and the formation is approximately 30 m thick. A 5-m-thick lens of coarse-grained sand occurs at the bottom of the formation and the well is completed in this lens. Similar lenses occur throughout the region and they are an important oil reservoir, so their location and thickness has been estimated by coring and well logs. The lens in the vicinity of well 9A is inferred to be approximately 1 km in lateral dimension (Figure 9), although the lateral extent is poorly constrained in several locations.

Well Test

A well test was conducted by injecting produced water into the well for approximately 6 days in 2017. Injection rates decreased from $9x10^{-4}$ to $5x10^{-4}$ m^3/s, and $7x10^{-4}$ m^3/s is the average rate. The injection rate also varied on a 5 hr period. Variations in injection rate occurred because the water supply for the test was controlled by infrastructure associated with the operating oil field.

Water pressure was measured at three observations wells and at three borehole strainmeters. The strainmeters are clustered between 210 and 220 m (r^* = 0.40 – 0.42) from well 9A at a location called AVN in Figure 9 and yellow dot in Figure 1. The strainmeters include a Gladwin strainmeter (*Gladwin*, 1984) and two new strainmeters of our design (*Murdoch et al*. 2019). One of the new strainmeters uses eddy-current sensors to measure horizontal and vertical strain, along with tilt. The other one measures the average horizontal strain using an optical fiber sensor. The Gladwin strainmeter measures the horizontal strain tensor. The strainmeters were grouted into a 3-m-thick limestone bed at a depth of 30m. Shale occurs below and above the limestone.

Pressures at observation wells 27, 29, and 60 were measured with submersible transducers (In-Situ Rugged Troll, https://in-situ.com/us/), which were retrieved after the test. The pressure measurements were corrected for changes in barometric pressure, and adjusted for long-term trends (*Murdoch et al.,* 2019). The Gladwin strainmeter was calibrated at the factory, and our strainmeters were calibrated in the lab. The strainmeters were also calibrated in the field using Earth tides. Data are available at http://ds.iris.edu/mda/2J/

Results

The results include analyses of the pressure signal at a depth of d = 530 m in the reservoir, and analysis of strain at a depth of 30 m from the AVN strainmeters. The average pumping rate is $Q = 7x10^{-4}$ m^3/s, water viscosity μ = 1 cP, and reservoir thickness b = 5 m.

Analysis of the pressure signal

Pressure at the monitoring wells was scaled to the distance from the injection well squared (Figure 10), which is a typical approach used to account for the effect of different radial distances on pressure data during well tests. The results indicate that data from wells 60 and 27 are similar to each other, whereas the data from well 29 are offset (Figure 10). There are two

intervals in each data set when the semi-log slope is roughly constant (red and blue lines in Figure 10). The intercept is in the range t_o/r^2= 0.6 to 0.7 s/m^2 for wells 60 and 27 and t_o/r^2 = 2 s/m^2 for well 29. This indicates values of hydraulic diffusivity of 0.7, 0.6 and 0.2 m^2/s using (23).

The results from the three monitoring wells indicate that the hydraulic diffusivity is D_h = 0.5 m^2/s ± 0.3 m^2/s. Using equation (15) with the semi-log slope from the data and estimates of Q, μ and b from above gives the permeability as k = 1x10^{-13} m^2 ± 0.6 x10^{-13} m^2. This value for k is within the range expected for the reservoir, which helps to confirm the interpretation of the pressure record. Those data indicate that the characteristic pressure is P_c = 1.3x10^{4}Pa, based on (7).

The intercept time, t_b, from the pressure data for wells 60 and 29 is approximately 3 x 10^{5}s, and it is approximately 4x10^{5}s based on the data from well 27 (fig. 4.28 in *Murdoch et al*. 2019). The slope increases by approximately a factor of 2 from the first to the second semi-log straight intervals. This indicates a mobility ratio of $M \approx 2$ based on (24). Assuming the fluid and solid compressibility and the layer thickness are uniform yields $D_{hR} = T_R = 2$. Then, $a = 2$ and it follows from (25) that $L_b \approx 220\ to\ 400$ m (Figure 9).

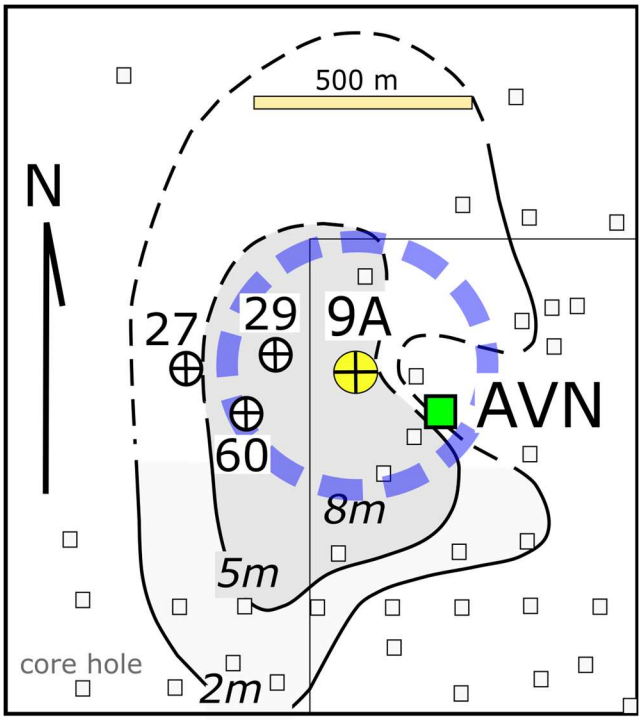

Figure 9. Isopach of thickness in meters of permeable lens at base of Bartlesville sand (*Robinowitz*, 2017). Thick purple dashed line is 300m from well 9A. Thin black line is the corner of Section 25 in T24N, R11E in northeastern Oklahoma.

Well 9A appears to be on the eastern side of a permeable lens, with a boundary approximately 100 to 300m to the east and an inferred boundary approximately 500 to 600 m to the west (Figure 9). This supports the conclusion that the change in slope in the pressure record from Well 60 is a result of interaction with the boundary of the lens. Moreover, it suggests that t_b and D_{h1} could be used to estimate the lateral extent of the lens, if cores or well logs were unavailable, for example.

Analysis of the strain signal

The horizontal strains become more tensile, whereas the vertical strain becomes more compressive with time as predicted by the theoretical analysis (Figure 4). Scrutiny of the record indicates that the horizontal and vertical strains approach semi-log straight lines, and they intersect in the range $0.7 < t_{oa}/r^2 < 0.9$ s/m^2. This indicates $0.5 < D_{h1} < 0.6$ m^2/s, which is within the range indicated by the pressure data from the monitoring wells, and it is also in the range of values expected for sandstone (e.g. *Barbour and Wyatt*, 2014, fig 11).

The finding in Figure 10b is consistent with the simulations (Figure 4) where the semi-log straight lines fit to ε_h and ε_{zz} intersect at the abscissa. The theoretical results indicate that the ratio t_{oa}/t_o is approximately equal to unity for $r^*>0.5$ (Figure 7). AVN is at approximately $r^* = 0.4$, but the data indicate that $t_{oa}/t_o \sim 1$ for this case. This suggests that t_{oa} from shallow strain data may be similar for radial distances slightly closer to the well than indicated by the idealized analysis used here.

The semi-log slope of the average horizontal strain, ε_h, is 65×10^{-9} to 75×10^{-9}, and the slope of the vertical strain is 95×10^{-9} to 105×10^{-9}. The transformational strain follows from these slopes using (21), which gives $\varepsilon_o = 3.0\ \mu\varepsilon \pm 0.2\ \mu\varepsilon$ from ε_h, and $\varepsilon_o = 2.9\ \mu\varepsilon \pm 0.2\ \mu\varepsilon$ from ε_{zz}. Measurements of ε_h and ε_{zz} are from instruments in two different boreholes, but they give essentially the same result for the transformation strain, ε_o.

The time, t_b, was determined for the average horizontal strain data to be approximately 3 x 10^5 s, and the semi-log slope approximately doubles from the first to the second straight-line intervals in the strain data (*Murdoch et al*. 2019, fig. 4.28). The results from the strain data indicate $L_b \approx 290$ to 320m. The first semi-log straight interval in the vertical strain data persists for the entire period of injection, which differs from the response of the horizontal strain and pressure.

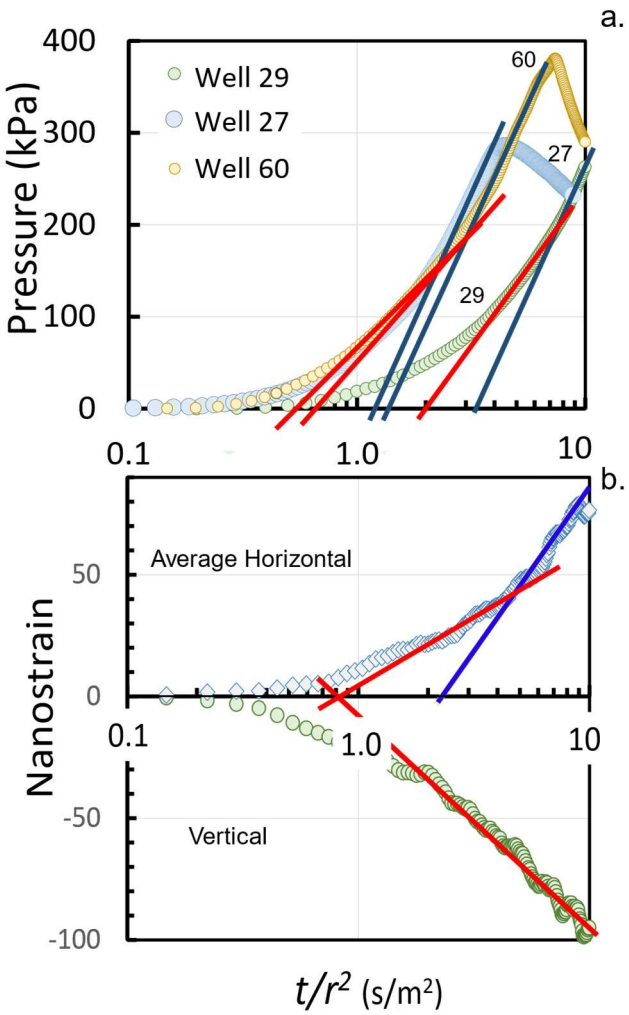

Figure 10. a.) Drawdown in monitoring wells 27, 29, and 60. b.) Average horizontal and vertical strain at AVN during injection test at well 9A. Red line is the best fit to first straight section, blue line is best fit to second straight section.

DISCUSSION

This work points out similarities between the pressure in an aquifer and strain field in the overlying confining unit.

Strain Field

Comparing equations (1) and (15) suggests that the thickness-averaged radial strain is proportional to the thickness-averaged pore pressure within the aquifer (reservoir). Such a local relation between the strain and pressure may be not very surprising as they are both measured at the same location. Our analyses indicate that there are time intervals when type-curves of strains and pressure both have substantial semi-log linear parts (Figures 4, 6a, 8a, 10). In other words, at such times, the strains measured above the reservoir are correlated to the aquifer pore pressure at the same radial distance from the injection well. Such a correlation

between deep pressure (measured inside the aquifer) and shallow strains (measured in the overlying layer) is unexpected and represents an important finding of this work.

It should be noted, however, that this observation may not be universal. In particular, it may not hold in the case of a thin aquifer and large diffusion times such that $\sqrt{D_{\mathrm{h}}t} \gg d \gg b$. In this case, the pressurization of the thin aquifer displaces the overlying layer by a vertical displacement, w, which is proportional to the local pore pressure, P, in the aquifer and can be written as [*Germanovich and Chanpura*, 2002; *Dyskin et al*., 1999]

$$w(r,t) = b\alpha P(r,t)/G \tag{27}$$

On the other hand, for $\sqrt{D_{\mathrm{h}}t} \gg d$, the overlaying layer can be treated as a thin plate when [e.g., *Timoshenko* and *Woinowsky-Krieger*, 1959]

$$\varepsilon_{rr} = -z\partial^2 w/\partial r^2,\ \varepsilon_{\theta\theta} = -(z/r)\partial w/\partial r,\ \ \varepsilon_{zz} = 0 \tag{28}$$

This implies that shallow strains in such confining unit are directly related to the aquifer pressure derivatives rather than pressure itself. Thus, in general, appropriate time intervals should be chosen for the type-curve analysis discussed in this work. Such intervals were, in fact, chosen in Figure 10, to analyze the North Avant Field results.

Implications

The analyses outlined above indicate that normal strain data measured at shallow depths can be used to estimate values of hydraulic diffusivity in the reservoir and the location of a lateral boundary (permeability barrier) that are similar to results from an analysis of pressures measured at a monitoring well completed in the reservoir. Results are consistent with characterization using cores from the vicinity and other well tests within the reservoir (Figure 9; *Murdoch et al.* 2019).

An important implication is that the strain data were measured at a depth of 30 m whereas the pressure data were measured in the reservoir at 530 m depth. This suggests that strain data measured at shallow depths outside of the reservoir or aquifer could provide characterization information that previously required the use of deep monitoring wells.

The importance of horizontal strain in the vicinity of wells has been recognized since the early measurements by *Wolff* (1970) and analyses by *Helm* (1994) and *Burbey (*1999), but there are scant examples of horizontal strain data used to interpret well tests. This is because measuring small horizontal strains has required specialized instruments that have been too cumbersome or expensive to justify using for well testing. Gladwin strainmeters were developed to measure horizontal strains for geodetic applications associated with plate tectonics, but their cost has limited hydrologic applications. A notable exception is the analysis of strains caused by pumping from wells near two Gladwin strainmeters (B082 and B089) by *Barbour and Wyatt* (2014). Those strainmeters were installed for tectonic studies, but two wells were located close enough to create strains that could be measured by B082 and B089, and *Barbour and Wyatt* (2014) recognized the opportunity to analyze these data for aquifer characterization.

Limitations on the accessibility of horizontal strain data for hydrologic applications may be easing. We have deployed an optical fiber strainmeter (*Murdoch et al*. 2019) and installed it next to the Gladwin strainmeter at the North Avant Field and the two instruments give essentially

the same results for ε_h (*Murdoch et al*. 2019). The new optical fiber strainmeter is based on a simple, robust design that can be constructed for a modest cost. Ongoing work (*Hua et al*. 2017 and 2020; *DeWolf et al*. 2020) is developing capabilities to measure multiple components of strain, and to measure strain in unconsolidated materials during well testing. Other groups, including *Becker at al*. (2017) and *Sun et al*. (2020) are evaluating the use of uniaxial strain measured with commercial interrogators during well testing. We are optimistic that optical fiber sensors hold the key to making multi-component strain measurements readily available for hydrologic analyses.

Interpretation of strain data during well testing will become increasingly important as in-situ strain measurement becomes more accessible (*Cappa,* et al. 2006; *Schuite et al*. 2017; *Murdoch et al*. 2020; *Sun et al*, 2020; *Zhang et al*. 2020). We envision that simple methods, like the ones described here, could provide initial estimates for more comprehensive analyses of strain data (*Vasco et al,* 2001; *Barbour and Wyatt*, 2014; *Schuite et al*, 2015, 2017; *Murdoch et al*. 2019). Future characterization efforts may replace one deep monitoring well with multiple shallow strainmeters, which could be used to improve the resolution of hydraulic tomography (e.g. *Bohling et. al*., 2007; *Illman et al*. 2009; *Cardiff and Barash*, 2011; *Tiedeman and Barash*, 2019) or related inversion methods. The tensor characteristics of strain may hold advantages beyond simply replacing pressure measurements in monitoring wells. For example, the time t_b determined from pressure data can constrain the distance to a boundary (eq. 25), but using multiple components of the strain tensor can constrain the location and orientation of the boundary, which has the potential to sharpen the resolution of inversions to characterize aquifers or reservoirs.

CONCLUSIONS

An approach for interpreting strain data measured in confining units during well tests was developed by comparing strains and pressures from poroelastic simulations to results from classic pressure type curves. The results indicate that characteristics of normal strains in the confining unit resemble characteristics of the pressure type curve. For example, time scales in a pressure record that can be used to estimate hydraulic diffusivity or distance to a boundary are essentially the same as the times determined from the record of average horizontal normal strain measured at $r^* > 0.5$. The approach was tested using field data from an injection test at a 530-m-deep reservoir. Pressure data from three monitoring wells indicate the hydraulic diffusivity is $D_h = 0.5 \pm 0.3$ m^2/s. Horizontal strain data from one instrument at 30-m depth, and vertical strain data from a different nearby instrument both give values of D_h within the range from the monitoring wells. The shallow strain data appear to respond to a lateral heterogeneity in the reservoir, suggesting that the approach can be used to characterize reservoir structure.

New developments in instrumentation promise to reduce costs and increase resolution of in situ strain measurements. It may be feasible, for example, to install multiple shallow strainmeters for the same cost as one deep monitoring well. The work presented here shows that a preliminary interpretation of shallow normal strain data can be straightforward, and it sets the stage for integrating strain data into future well testing projects.

ACKNOWLEDGEMENT

We appreciate financial support from U.S. Department of Energy projects DE-FE0023313 and DE-FE0004542. The content of this paper is the responsibility of the authors. The U.S.

Department of Energy bears no responsibility for the contents of this paper. We appreciate logistical support and access to the North Avant Field provided by Marvin and Scott Robinowitz, Grand Resources Inc. Data are available at http://ds.iris.edu/mda/2J/ .

REFERENCES

Bear, J., Corapcioglu, M.Y., 1981. Mathematical model for regional land subsidence due to pumping, 2. Integrated aquifer subsidence equations for vertical and horizontal displacements, Water Resour Res, 17 (4) 947–958.

Becker, M., Ciervo, C., Cole, M., Coleman, T., Mondanos, M. (2017) Fracture Hydromechanical Response Measured by Fiber Optic Distributed Acoustic Sensing at milliHertz Frequencies: Fracture Hydromechanics from DAS. Geophysical Research Letters, v44. 10.1002/2017GL073931.

Bohling, G.C., J.J. Butler Jr., X. Zhan, and M.D. Knoll. 2007. A field assessment of the value of steady shape hydraulic tomography for characterization of aquifer heterogeneities. *Water Resources Research* **43**: W05430. https://doi.org/10.1029/2006WR004932

Bourdet, D., Ayoub, J.A., Pirard, Y.M. (1989) Use of pressure derivatives in well test interpretation. Society of Petroleum Engineers, Formation Evaluation. V. 4. 02, June. https://doi.org/10.2118/12777-PA.

Barbour, A. J., and F. K. Wyatt (2014), Modeling strain and pore pressure associated with fluid extraction: The Pathfinder Ranch experiment, J. Geophys. Res. Solid Earth, 119, 5254–5273, doi:10.1002/2014JB011169.

Burbey, T J., (1999) Effects of horizontal strain in estimating specific storage and compaction in confined and leaky aquifer systems: Hydrogeology Journal, v. 7, no. 6., pp. 521-532.

Cappa, F., Guglielmi, Y., Gaffet, S., Lançon, H., & Lamarque, I. (2006). Use of in situ fiber optic sensors to characterize highly heteroge-neous elastic displacement fields in fractured rocks. International Journal of Rock Mechanics and Mining Sciences, 43(4), 647–654.Cardiff, M.A., and W. Barrash. (2011) 3-D transient hydraulic tomography in unconfined aquifers with fast drainage response. *Water Resources Research* **47**: W12518 https://doi.org/10.1029/2010WR010367

Cooper, H.H., and Jacob, C.E. (1946) A generalized graphical method for evaluating formation constants and summarizing well field history, Am. Geophys. Union Trans., vol. 27, pp. 526-534.

DeWolf, S., L.C. Murdoch, L.N. Germanovich, R. Moak, M. Furgeson. (2019) Designs and Results from Three New Borehole Optical Fiber Tensor Strainmeters. AGU Fall Meeting, S21G-0597.

Detourney, E., and Cheng, A.H.D. (1993), Fundamentals of Poroelasticity, Journal of Fluid Mechanics, pp. 113-177.

Dyskin, A. V., Germanovich, L. N., and Ustinov, K. B., 2000, Asymptotic analysis of crack interaction with free boundary, *International Journal of Solids and Structures*, Vol. 37, No. 6, pp. 857 – 886.

Earlougher, R.C., Jr. (1977), Advances in well test analysis. Monograph Series 5, SPE, Dallas,

516 TX.

517 Eshelby, J. D. (1957) The determination of the elastic field of an ellipsoidal inclusion, and other
518 related problems, Proc. R. Soc. London, Ser. A, 241, 376 – 396.

519 Ferris, J.G., D.B. Knowles, R.H. Brown and R.W. Stallman, (1962) Theory of aquifer tests, U.S.
520 Geological Survey Water-Supply Paper 1536 E, 174p.

521 Germanovich L. N., and Chanpura, R. A., 2002, Modeling Thin Inclusions in Poroelastic
522 Medium by Line Discontinuities, *IUTAM Symposium on Analytical and Computational*
523 *Fracture Mechanics of Non-Homogeneous Materials*, B. L. Karihaloo (ed.), Kluwer,
524 Dordrecht, Boston, London, pp. 133 – 142.

525 Gringarten, A. C. (1987). Type-Curve Analysis: What It Can and Cannot Do. Society of
526 Petroleum Engineers, v. 39 n.1. doi:10.2118/16388-PA.

527 Hantush, M.S. (1960), Modification of the theory of leaky aquifers. J. Geophys. Res. 65, 3713-
528 3725.

529 Helm, D.C. (1994). Horizontal aquifer movement in a Theis-Thiem confined system. Water
530 Resources Research, V. 30, N. 4 , P. 953-964. https://doi.org/10.1029/94WR00030

531 Hua, L. Yang Song, Baokai Cheng, Wenge Zhu, Qi Zhang, and Hai Xiao, (2017) Coherence-
532 length-gated distributed optical fiber sensing based on microwave-photonic
533 interferometry, Opt. Express 25, 31362-31376

534 Hua, L. X. Zhu, S. DeWolf, J. Lei, Q. Zhang, L. Murdoch, and H. Xiao. (2020) Phase
535 demodulation by Frequency Chirping in Coherence Microwave Photonic Interferometry.
536 IEEE Journal of Selected Topics in Quantum Electronics, DOI:
537 10.1109/JSTQE.2020.2975575.

538 Illman, W.A., X. Liu, S. Takeuchi, T.-C.J. Yeh, K. Ando, and H. Saegusa. (2009) Hydraulic
539 tomography in fractured granite: Mizunami underground research site, Japan. Water
540 Resources Research 45: W01406. DOI:10.1029/2007WR006715

541 Kruseman, G.P., and de Ridder, N.A. (1970), Analysis and evaluation of pumping test data.
542 International Institute for Land Reclamation and Improvement, Wageningen, The
543 Netherlands.

544 Matthews, C.S., and Russell, D.G. (1967), Pressure Buildup and Flow Tests in Wells. Soc. of
545 Pet. Engineers of AIME. 1-155

546 Muskat, M. (1937), The flow of fluids through porous media. Journal of Applied Physics. vol. 8,
547 274-282.

548 Murdoch, L.C, Scott DeWolf, Leonid Germanovich, Alex Hanna, Robert Moak and Stephen
549 Moysey. (2019). Characterizing and Interpreting the In Situ Strain Tensor During CO2
550 Injection. Final Report for DOE Project DE-FE 0023313, 252 p.

551 Murdoch, L.C. L. N. Germanovich, S. J. DeWolf, S.M.J. Moysey, A.C. Hanna, S. Kim, R.G.
552 Duncan, (2020). Feasibility of Using In Situ Deformation to Monitor CO_2 Storage.
553 International Journal of Greenhouse Gas Control, v. 93. 102853.
554 https://doi.org/10.1016/j.ijggc.2019.102853.

555 Reed, J.E., 1980, Type curves for selected problems of flow to wells in confined aquifers.

Techniques of Water-Resources Investigations of the United States Geological Survey, Book 3, Chapter B3, US Government Printing Office, Washington D.C., 106 p, https://pubs.usgs.gov/twri/twri3-b3/pdf/TWRI_3-B3.pdf.

Robinowitz, S. 2017. Isopach map from vicinity of Well 9A from internal data obtained by Grand Resources Inc.

Schuite, J., L. Longuevergne, O. Bour, F. Boudin, S. Durand, and N. Lavenant (2015), Inferring field-scale properties of a fractured aquifer from ground surface deformation during a well test, Geophys. Res. Lett., 42, 10,696–10,703, doi:10.1002/2015GL066387.

Schuite, J., L. Longuevergne, O. Bour, N. Guihéneuf, M. W. Becker, M. Cole, T. J. Burbey, N. Lavenant, and F. Boudin (2017), Combining periodic hydraulic tests and surface tilt measurements to explore in situ fracture hydromechanics, J. Geophys. Res. Solid Earth, 122, 6046–6066, doi:10.1002/2017JB014045.

Streltsova, T.D. (1988), Well Testing in Heterogeneous Formations, xxvii+413 pp. New York, Chichester, Brisbane, Toronto, Singapore: John Wiley. ISBN 0 471 63169 8.

Sun, Y., Xue, Z., Hashimoto, T., Lei, X.,& Zhang, Y. (2020). Distributed Fiber Optic Sensing System for Well-Based Monitoring Water Injection Tests—A Geomechanical Response Perspective..Water Resources Research, 56,e2019WR024794. https://doi.org/10.1029/2019WR024794

Teideman, C.R., W. Barash (2019) Hydraulic Tomography: 3D Hydraulic Conductivity, Fracture Network, and Connectivity in Mudstone. Vol. 58, No. 2, p. 238‐257. https://doi.org/10.1111/gwat.12915

Theis, C.V. (1935), The relation between the lowering of the piezometric surface and rate and duration of discharge of a well using groundwater storage. Trans. Am. Geophys. Union 2, 519-524.

Timoshenko, S.P. and Woinowsky-Krieger, S., *Theory of Plates and Shells*, 2nd edn,. McGraw-Hill, New York, 1959.

Vasco, D. W., K. Karasaki, and K. Kishida (2001), A coupled inversion of pressure and surface displacement, Water Resour. Res., 37(12), 3071–3089.

Verruijt, A., 1969. Elastic storage of aquifers. In: R.J.M. De Wiest (Editor), Flow Through Porous Media. Academic Press, New York, pp. 331–376.

Wang, H.F. (2000), Theory of Linear Poroelasticity with Applications in Geomechanics and Hydrogeology, Princeton University Press, Princeton series in geophysics, pp. 72-76.

Wolff, R. G. (1970) Relationship between horizontal strain near a well and reverse water level fluctuation, *Water Resour. Res*., 6, 1721-1728.

Zhang, Y., X. Lei3 , T. Hashimoto, Z. Xue (2020) In situ hydromechanical responses during well drilling recorded by distributed fiber-optic strain sensing. Solid Earth, 11, 2487–2497, https://doi.org/10.5194/se-11-2487-2020.